Journal of Materials Chemistry A

Accepted Manuscript

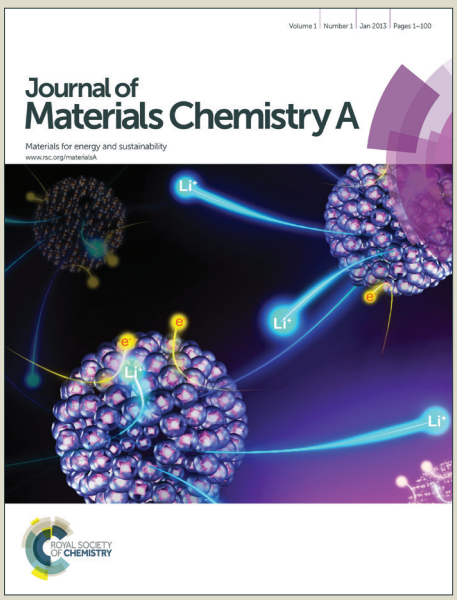

ROYAL SOCIETY OF CHEMISTRY

www.rsc.org/materialsA

Ab initio study of doping effects on $LiMnO_2$ and Li_2MnO_3 cathode materials for Li-ion batteries

Fantai Kong,[†] Roberto C. Longo,[†] Min-Sik Park,[‡] Jaegu Yoon,[‡] Dong-Hee Yeon,[‡] Jin-Hwan Park,[‡] Wei-Hua Wang,[†] Santosh KC,[†] Seok-Gwang Doo*[,‡] and Kyeongjae Cho*[,†]

[†]Materials Science & Engineering Dept., The University of Texas at Dallas, Richardson, TX 75080, United States

[‡]Energy Lab., Samsung Advanced Institute of Technology, Samsung Electronics, Yongin 446-712, Republic of Korea

KEYWORDS: $LiMnO_2$, Li_2MnO_3, doping, polaron, high voltage cathodes, Li-ion battery

Ⓢ *Supporting Information*

ABSTRACT: For the over-lithiated-oxides (OLOs), a composite of layered Li_2MnO_3 and $LiMO_2$ (M = Mn, Co, Ni), the Li_2MnO_3 part is not stable after the 1st charge-discharge cycle and partly transforms into layered $LiMnO_2$, which in practice indicates that the phase used is actually a mixture of both Li_2MnO_3 and $LiMnO_2$. In the present work, the influences of 10 cationic (Mg, Ti, V, Nb, Fe, Ru, Co, Ni, Cu, Al) and 2 anionic (N, F) dopants on the phase stability, redox potential, ionic and electronic conductivity of both Li_2MnO_3 and $LiMnO_2$ are investigated in detail using density functional theory. The calculations show that all the cationic dopants and F can be thermodynamically stable into the layered structures. The redox potential of both oxides is quite sensitive to some of the dopants, like V, Nb, Ru, due to the appearance of gap states introduced by those dopants. The Jahn-Teller effect has a strong influence on the Li vacancy diffusion behavior in both $LiMnO_2$ and its doped phases. Li vacancy diffusion behavior in Li_2MnO_3, including both interlayer and intralayer pathways, is relatively more complex and some dopants like Mg, Ti, Nb, Ru can decrease the barriers of the diffusion paths. The calculations also show the evidences of hole polaron formation in $LiMnO_2$ and electron polaron formation in Li_2MnO_3 which should be the reason why these phases have low electronic conductivities. Based on these findings, possible ways to improve the electronic conductivity through the doping process are discussed.

INTRODUCTION

Driven by the growing demand for clean-efficient energy storage medium, Li-ion batteries have been widely studied and applied in cell phones, portable computers, electric vehicles, etc. $LiCoO_2$ is the earliest commercialized cathode material for Li-ion batteries, with a redox potential around 4 eV. However, only half of the Li in $LiCoO_2$ can be extracted, in order to ensure the structural and chemical stability. $LiCoO_2$ therefore provides a low practical capacity of up to 140 $mAh \cdot g^{-1}$.[1,2] Another kind of layered oxide, $LiNiO_2$, which contains much cheaper Ni, showed higher cycling life, but still slightly improved the capacity to ~170 $mAh \cdot g^{-1}$.[3,4,5] Mixed layered compounds, such as $LiCo_xNi_{1-x}O_2$ and $LiMn_xNi_{1-x}O_2$, can also help to cut down the preparation cost but not to improve the phase instability problem and they also only slightly increase the capacity.[6,7,8] On the other hand, the fabricated olivine-type $LiFePO_4$ is shown to have very good phase stability and low cost, but with a maximum practical capacity of 170 $mAh \cdot g^{-1}$ and a redox potential as low as 3.4 V,[9,10,11] making this compound inappropriate for applications where high energy density is required.

During the past decade, the over-lithiated-oxides (OLOs), a composite of layered structures of Li_2MnO_3 and $LiMO_2$ (M = Mn, Co, Ni), have been shown to deliver a theoretical capacity of ~300 $mAh \cdot g^{-1}$ and realistic capacity of 200~250 $mAh \cdot g^{-1}$ which is higher than traditional layered oxides as Li ion battery cathode materials. The Li_2MnO_3 phase is the source providing extra Li ions, thus playing a dominant role in determining the high capacity. However, experimental work has found a voltage plateau when charged to over 4.4 V during the 1st charge cycle.[12] Several mechanisms have been proposed to explain this phenomenon. Robertson et al proposed a charging model with the initial Li accompanied by oxygen loss and further exchange with proton in the electrolyte.[13,14] Following experiments observed O_2 evolution on the surface and the formation of Li_2O and Li_2CO_3, based on

which a two-step mechanism is provided: first, there is oxygen loss on the surface in the form of Li_2O and Li_2CO_3; second, a lattice densification through the migration of $Mn^{3+/4+}$ ions to the neighboring Li vacancy sites, that is, the formation of a $LiMnO_2$ phase.[5,15,16,17] A recent work also proposed that, following the densification process, an oxygen oxidation process could also happen within the bulk.[18] Therefore, the practically used oxide can be viewed as a mixture of both $LiMnO_2$ and Li_2MnO_3 phases.

In real applications, these cathode materials are often doped in an attempt to optimize their properties. For example, it has been shown that, by doping $LiMnO_2$ with Zn, Fe, Co, Cr or Al, better capacity retention or higher discharge capacity can be obtained.[19,20] low concentration of Cr doping improves the capacity and lithium diffusion in Li_2MnO_3[21] and Ru-doped Li_2MnO_3 shows higher electronic conductivity and cycling stability.[22,23] In this work, we conduct a systematic study to analyze the influence of 10 cationic dopants (Mg, Ti, V, Nb, Fe, Ru, Co, Ni, Cu, Al) and 2 anionic dopants (N, F) on the electrochemical properties of both Mn oxide cathode materials, using *ab initio* density-functional theory (DFT) simulations. The first property is thermodynamic phase stability, which to a large extent determines whether the doped-Mn oxides can form stable phases. Redox potential is another electrochemical property of interest. An intermediate redox potential is preferred since a too high value will increase the interlayer instability and a too low value will not provide the required device voltage. Lithium ion diffusion is also an important property, closely related to the battery charge-discharge efficiency. Last, the electronic conductivity determines the power performance of the battery. The electronic conductivities of both oxides, especially the Li_2MnO_3 phase, are quite low in comparison with similar layered structures as $LiNiO_2$ and $LiCoO_2$. The measured electronic conductivity of Li_2MnO_3 is as low as 10^{-9} S/cm at 300K.[22,24] Although no direct electronic conductivity data for $LiMnO_2$ has been reported, the value can be estimated to be around 10^{-4}~10^{-5} S/cm from the available data of $NaMnO_2$ and $KMnO_2$ at 300K.[25] However, the electronic conductivities of $LiNiO_2$ and $LiCoO_2$ are 10^{0}~10^{-1} and 10^{-2}~10^{-3} S/cm, respectively.[26,27,28] The reason of the low conductivity of Li_2MnO_3 was in principle attributed to its large band gap (around 1.5~2.0eV), but the band gap of $LiCoO_2$ is actually even larger as 2.7 eV[29]. This indicates that the band gap itself may not explain the difference and some hidden mechanism must exist. From the present work, evidence from the electronic structure seems to indicate that the reason for low electronic conductivity can be largely attribute to the formation of charge polarons.

To avoid the misunderstanding that changes of properties of materials in our simulation due to doping are just local to dopant, but not overall properties of the materials, we want to clarify that, in battery materials, elemental substitution described as 'doping' can be introduced up to a few %, sometimes 30%~50% for some specific purposes,[19,22,44] which is quite different from the parts *per* million (p.p.m.) level doping in electronic device materials used to control electronic carrier concentrations in semiconductors. Even though the battery materials community uses the terminology 'doping' to describe element substitution (e.g., Ni and Al substitution of Co in $LiCoO_2$ to form $LiNi_{0.15}Co_{0.8}Al_{0.05}O_2$ (NCA)), it does not imply small amount as in electronic device material doping. For this reason, the amount of doping (more precisely, element substitution) is required to be large enough to change the overall electrochemical properties of the battery materials.

COMPUTATIONAL METHODS

The present work is performed using the Vienna ab initio simulation package (VASP)[30,31] within the projector-augmented wave (PAW) method[32]. The generalized gradient approximation Perdew-Burke-Ernzerhof (GGA-PBE) exchange and correlation functional is selected for all the calculations.[33] After the corresponding accuracy test, a plane wave cutoff energy of 500 eV is employed throughout all the study. The structure optimization is carried out using a conjugate-gradient algorithm until the forces on each atom are less than 0.02 eV/Å and the total energy is converged up to 10^{-4} eV. The self-consistent calculations are performed under the tetrahedron method with Blöchl corrections[34] with an energy convergence criteria of 10^{-5} eV. As is widely known that the localized nature of 3d electrons is hard to be accurately described by GGA, we also employed the effective on-site Hubbard U_{eff} correction on the 3d or 4d electrons for all the transition metals included in our calculations.[35] The U_{eff} parameter was taken from previous theoretical reports: 4.2 eV, 3.0 eV, 3.0 eV, 5.0 eV, 4.2 eV, 2.9 eV, 4.0 eV, 6.4 eV, 5.2 eV for Ti, V, Nb, Mn, Fe, Ru, Co, Ni, Cu respectively. [35-47]

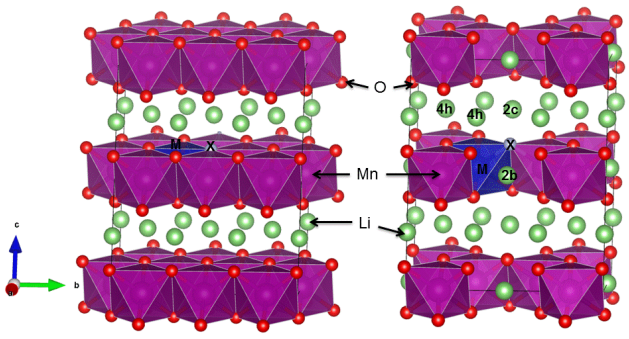

Figure 1. Modeling configurations of $LiMnO_2$ (left) and Li_2MnO_3 (right), with the blue atom (M) marking cationic dopants and grey atom (X) for anionic dopants.

For the thermodynamic stability and ionic conductivity calculations, we selected supercells containing 8 unit cells, i.e., $Li_{12}Mn_{12}O_{24}$ and $Li_{16}Mn_8O_{24}$. The doping is realized by replacing one $Mn^{3+/4+}$ ion with one cation M (M = Mg, Ti, V, Nb, Fe, Ru, Co, Ni, Cu, Al) or one O^{2-} ion with one anion X (X = N, F). Therefore, the doped phases would correspond to the $LiMn_{0.917}M_{0.083}O_2$, $Li_2Mn_{0.875}M_{0.125}O_3$, $LiMnO_{1.917}X_{0.083}$ and $Li_2MnO_{2.875}X_{0.125}$ stoichiometries, respectively. The selected supercell and doping positions are illustrated in Figure 1. For $LiMnO_2$, all the Li sites have the same chemical environment, whereas for Li_2MnO_3, there are three different Li atomic sites, due to the presence of Li atoms in the Mn layer. The three sites, 2b, 2c and 4h are shown in Figure 1. All the structural figures were plotted using the VESTA software.[48] The nudged elastic band (NEB) method is adopted to find the kinetic energy barrier along the Li diffusion pathways.[49]

For the polaron calculations, a larger supercell of 16 unit cells, i.e., $Li_{24}Mn_{24}O_{48}$ and $Li_{32}Mn_{16}O_{48}$ is used in order to avoid the polaron-polaron interactions between neighboring images. To generate the necessary extra charge carriers in the system, one electron is added or removed from the neutral system. To avoid the coulomb divergence problem, a homogeneous positive or negative background charge is added to compensate the extra charge.

RESULTS AND DISCUSSION

a. Thermodynamic stability. We first studied the thermodynamic stability of the doped Mn oxides, in order to see whether a particular dopant can lead to a thermodynamically stable structure. During the synthesis process, the dopant element *M* is firstly contained in precursors like $M(CH_3COO)_x$, $M(COO)_x$, $M(NO_3)_x$ *etc* [19,20,21] or even directly in the oxide form, for example RuO_2 [22]. The precursors will afterwards react chemically during the calcination process under air environment, plenty of O_2. For this reason, the dopant may form stable MO_x or similar layered lithiated oxides $LiMO_2$, instead of occupying Mn sites in $LiMnO_2$ or Li_2MnO_3. Taking into account the Li vaporization during the annealing process, excess Li is often provided in order to ensure the stoichiometry of the final compound after calcination process. To model such Li-rich environment, bcc bulk Li is used as the reference state. Within these considerations, we should compare the phase stability between *M* oxides (MO_x or $LiMO_2$) and *M* doped Li_xMnO_y oxides and, then, derive the thermodynamic stability of each doped structure in terms of the calculated heat of formation, which have been obtained using the following formula, where $E(A)$ is the DFT-total energy of the structure *A*.

$$H_{f,Li_{16}Mn_7M_1O_{24}} = E(Li_{16}Mn_7M_1O_{24}) - 7*E(Li_2MnO_3) - E(LiMO_2) - E(Li) - \frac{1}{2}E(O_2)$$

$$H_{f,Li_{16}Mn_8O_{23}X_1} = E(Li_{16}Mn_8O_{23}X_1) + \frac{1}{2}E(O_2) - 8*E(Li_2MnO_3) - \frac{1}{2}E(X_2)$$

$$H_{f,Li_{16}Mn_7M_1O_{24}} = E(Li_{16}Mn_7M_1O_{24}) - [7E(Li_2MnO_3) + 2E(Li) + \frac{3-x}{2}E(O_2) + E(MO_x)]$$

$$H_{f,Li_{12}Mn_{11}M_1O_{24}} = E(Li_{12}Mn_{11}M_1O_{24}) - 11*E(LiMnO_2) - E(LiMO_2)$$

$$H_{f,Li_{12}Mn_{12}O_{23}X_1} = E(Li_{12}Mn_{12}O_{23}X_1) + \frac{1}{2}E(O_2) - 12*E(LiMnO_2) - \frac{1}{2}E(X_2)$$

$$H_{f,Li_{12}Mn_{11}M_1O_{24}} = E(Li_{12}Mn_{11}M_1O_{24}) - [11E(LiMnO_2) + E(Li) + \frac{2-x}{2}E(O_2) + E(MO_x)]$$

The meaning of the heats of formation of the different phases can be understood as a measure of their relative stability with respect to the corresponding reference state. The bulk Lithium BCC metal with space group Fm-3m and O_2 gas phase are selected as the reference phases of Li and O, respectively. For Al, Cu, Mg, Ru, Ti, V, Fe, their most stable oxides are chosen as the reference states: Al_2O_3 (R-3cR), CuO (C12/c1), MgO (Fm-3m), RuO_2 (P42/m nm), TiO_2 (P42/m nm), V_2O_5 (Pmmn) and Fe_2O_3 (R-3cR). Nb, Co and Ni show stable layered $LiMO_2$ (M=Nb, Co, Ni) phases, which are therefore selected as the corresponding reference states. For the anionic dopants N and F, we chose the gas phases N_2 and F_2 as the reference states.

The calculated heats of formation are shown in Figure 2. The picture shows that H_f of almost all the cationic doped phases is negative, indicating that the cationic dopants can replace Mn ions in both layered oxides without phase separation. The picture also shows that H_f of all the cation-doped Li_2MnO_3 compounds is lower than the corresponding H_f of the $LiMnO_2$ compounds, indicating that the cationic doped Li_2MnO_3 phase is more stable. This finding is consistent with the fact that orthorhombic $LiMnO_2$ is the most stable structure in equilibrium conditions and the layered monoclinic $LiMnO_2$ is metastable between rhombus and spinel.[20] For the anionic doping, N doped $LiMnO_2$ and Li_2MnO_3 phases is unlikely to be synthesized in the laboratory, due to a positive heat of formation of around 0.5 eV/f.u.. This result is explained by the strong bonding of the N_2 molecules and their well-known tendency to nucleate. The F doped phases are thermodynamically stable, although with a value of H_f only slightly negative for $LiMnO_2$ and almost zero for Li_2MnO_3. These results for H_f are consistent with the experimental evidence, because synthesized Fe doped $LiMnO_2$[19] and Fe, Ti, Ru and Al doped Li_2MnO_3 phases[21,22,23,50] are shown to be stable and they can also improve some of the electrochemical properties of the pure materials. To the best of our knowledge, there is no experimental report about anionic doping in layered $LiMnO_2$ and Li_2MnO_3, but fluorine doped *o*-$LiMnO_2$ and $Li_{1.27}Cr_{0.2}Mn_{0.53}O_2$ has been shown to be thermodynamically stable.[51,52] Considering that GGA gives an overbinding energy of 1.36 eV per O_2 molecule, as compared to the experimental data,[41] we have calculated how it affects the heat of formation. Our results indicate a small energy shift of 0.05~0.17 eV/f.u., but the overall conclusions are not affected. Also, to test the accuracy of the obtained heats of formation using GGA+U, we also performed additional tests for some selected systems

using the HSE hybrid functional.[53] Our results show that the heats of formation of Mg, Al and Ni-doped $LiMnO_2$ are, -1.37, -1.27 and -0.88 eV, respectively (as compared to the GGA+U obtained values of -0.79, -0.65 and -0.33 eV, respectively). Therefore, the energy shift in the obtained heats of formation is relatively similar for all the doped phases studied and does not affect the main conclusions of this work.

In order to examine the possibility of a dopant-induced layered-to-spinel phase transition, we have performed additional calculations of the formation energies on the Fe, Nb and Cu-doped spinel $LiMn_2O_4$ phase and compared the results with those of the corresponding $LiMnO_2$ and Li_2MnO_3 systems. As shown in Table S1, doped spinel phase is always thermodynamically less favorable than the corresponding layered oxides. Also, XRD data has shown that Fe-doped $LiMnO_2$ keeps its layered structure up to 20% of Fe concentration.[19] No phase transition was observed in Ru-doped Li_2MnO_3 within the whole doping range studied[22] and XRD patterns confirmed the formation of a monoclinic Li_2MnO_3 layered structure after replacement of 30% of Mn atoms by Ti or Fe.[50]

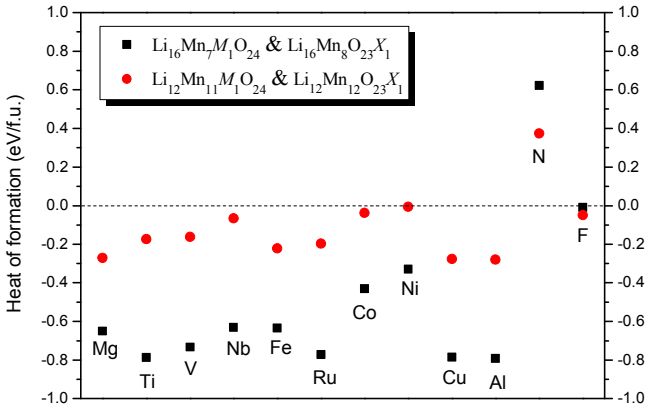

Figure 2. Heat of formation for doped $LiMnO_2$ and Li_2MnO_3.

b. Redox potential. The redox potential describes the energy needed to extract the Li out of the battery materials. The present results were obtained according to the following formula, where we considered the redox potential of extracting one Li atom:

$$V_{ave} = \frac{E(Li_{11}Mn_{11}M_1O_{24}) + E(Li) - E(Li_{12}Mn_{11}M_1O_{24})}{e}$$

$$V_{ave} = \frac{E(Li_{15}Mn_7M_1O_{24}) + E(Li) - E(Li_{16}Mn_7M_1O_{24})}{e}$$

The obtained results for doped LiMnO2 and Li_2MnO_3 are shown in Figs. 3(a) and 3(b), respectively. For pure $LiMnO_2$, the redox potential is calculated to be 3.67 V, which is represented by the blue dotted line in Figure 3(a), to allow the comparison with the doped phase. The obtained redox potential is similar to a previous calculation using the CASTEP code[54] that yielded a result of 3.75 V. The red dots represent the average redox potential of extracting the nearest neighbor Li and farthest neighbor Li ions to the dopant ("error bar" indicates the redox potential at these two different locations). The results show that most of the dopants facilitate the extraction of Li at lower voltage, except Co, which increases the potential by about 0.07 V. Mg, Ti, V, Nb, Ru and F have very remarkable effects in lowering the redox potential. The "error bar" also indicates such effect is not localized to the dopants. For instance, Ti lowers the redox potential by almost 1.10 V on average. Specifically, the redox potential to extract the nearest Li ion is 2.51 V, whereas the potential required to extract the farthest Li ion is 2.63 V. These results show that, for the supercell used in our calculations, which corresponds to a doping concentration of 8.33%, the influence of the dopant on the redox potential is effective over the whole structure.

For pure Li_2MnO_3, the redox potential of extracting Li ions from a Li only layer and a mixed Li-Mn layer are 4.61 V and 4.76 V respectively, in agreement with previous theoretical results.[38,55] Similar to Figure 3(a), they are represented as red and blue dotted lines, respectively, in Figure 3(b). The blue square points and red round points represent the average redox potential of extracting the nearest and farthest neighbor Li ion to the dopant in the Mix-layer and Li-layer, respectively. It can be seen that the influence of Mg, Ti, Co, Ni, Cu and Al dopants on the redox potential is negligible. However, V, Nb, Fe, Ru and F show a strong effect in lowering the redox potential. Especially remarkable is the case of Nb, where the redox potential is decreased by almost 2.5 V. It has been reported that, for the 1st cycle charge curves of $Li_2Mn_{0.99}Al_{0.01}O_3$ and $Li_2Mn_{0.99}Fe_{0.01}O_3$, Al has almost no influence on the redox potential while Fe decreases the potential by about 0.2 V.[21] That tendency is qualitatively consistent with our present calculations. The quantitative difference is also reasonable, given that we are modeling a much higher doping concentration. Another interesting example is the Ru doped Li_2MnO_3, whose redox potential is decreased up to 3.7 V, when 10% of Mn is substituted by Ru.[22] This experimental result is also in accordance with our result of 3.4 V, with 12.5% of Ru doping. On the other hand, as derived from Figure 3(b), Li ions are harder to extract from the Li-Mn mixed layer of pure Li_2MnO_3, 0.15 V. While Mg, Ti, Al decrease such potential difference, V and Ru make the Li extraction potential indistinguishable for both types of layers. For Nb doping, the redox potential is even lower for the Li-Mn mixed layer. Therefore, the aforementioned dopants will facilitate the extraction of Li ions from the Li-Mn mixed layer.

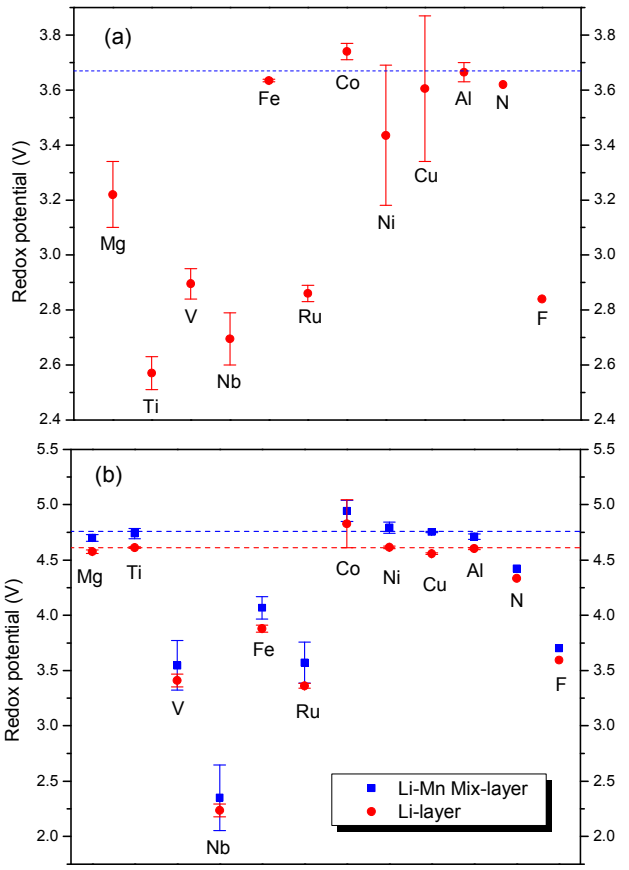

Figure 3. Redox potential for doped $LiMnO_2$ (a) and Li_2MnO_3 (b).

Regarding the physical origin to the lowering of the redox potential induced by the dopants, it should be pointed out that, during the extraction of Li atoms in the charging process, Li^+ ions diffuse through the electrolyte whereas the electrons diffuse through the external circuit. This fact implies that the facilitation of Li extraction by any external dopant is related with either a change in the distortions left by the Li^+ ion when extracted or a change in the electron chemical potential of the system. Our results have shown that the energy to extract the Li is independent of its distance to the dopant, *i.e.*, the effect on the distance of the Li^+ ion to the dopant must be weak. The influence of the dopant on the electron chemical potential can be understood from their electronic density of states (DOS), as shown in Fig. 4. The picture shows the examples of Fe, Ti and F doped $LiMnO_2$ and Li_2MnO_3. On the other hand, Fig. 3 shows that Fe and Ti doping have a strong influence in the redox potential of Li_2MnO_3 and $LiMnO_2$, respectively, and that F doping shows a strong effect on both oxide phases. Figure 4 shows that, when the doping lowers the redox potential, the Fermi level shifts beyond the valence band maximum (VBM), also passing through the gap states, which indicates an increase of the electron chemical potential, thus facilitating the removal of the electron and, consequently, the Li atom. These gap states are always contributed by either the dopant-oxygen (M-O) bonding or Mn-O bonding, indicating different electrochemically activated atoms in different doped phases to compensate the Li extraction. More specifically, in V and Ru doped $LiMnO_2$, gap states are composed by dopant-O bonding, meaning that V and Ru are electrochemically activated during the Li extraction. Whereas for Mg, Ti, Nb and F doped $LiMnO_2$, gap states are composed by Mn-O bonding, indicating a redox active dopant-induced Mn *d*-orbitals splitting during the Li extraction. For the V, Fe and Ru doped Li_2MnO_3 phase, the gap states are mainly contributed by dopant-O bonding, which means that V, Fe and Ru are the electrochemically active atoms. On the contrary, Nb and F induce Mn-O bonding *d*-orbitals splitting, with the subsequent formation of gap states.

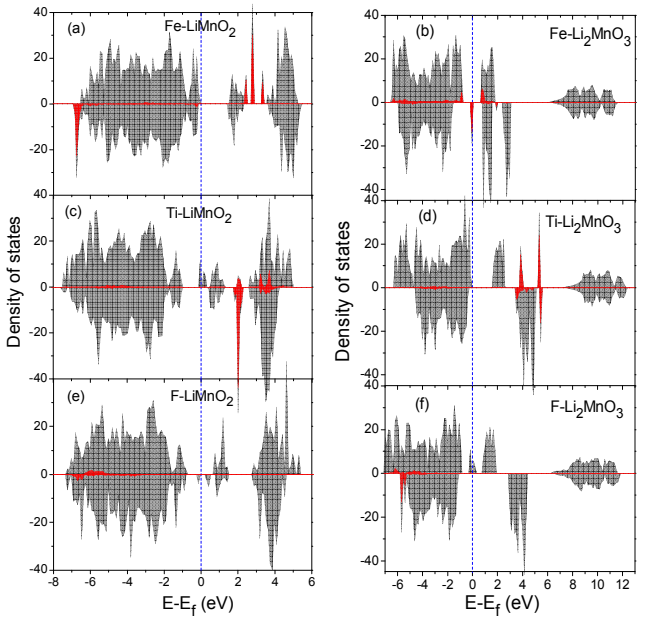

Figure 4. Density of States of (a) Fe doped $LiMnO_2$, (b) Fe doped Li_2MnO_3, (c) Ti doped $LiMnO_2$, (d) Ti doped Li_2MnO_3, (e) F doped $LiMnO_2$ and (f) F doped Li_2MnO_3. The grey region represents the phase total density of states and the red region is the dopant density of states.

The above calculations reveal that some dopants have strong effect in lowering the redox potential of extracting one Li out of the system, which represents the initial charging range. While the simulation of the extraction of the second Li in our model indicates that redox potential of these doped phases will be restored to pure $LiMnO_2$ or Li_2MnO_3 (as shown in Table S2). The only exception is the Nb doped $LiMnO_2$, where an intermediate value of 3.03 V is found when extracting the second Li. As a summary, a 8.33% doping concentration of Mg, Ti, V, Ru or 4.17% F in $LiMnO_2$ have the effect of lowering the redox potential of the initial 8.33% Li by 0.4~1.0 V. Nb in $LiMnO_2$ has wider effect that can lower the redox

potential of 16.67% Li, with the first 8.33% of 2.70 V and the following 8.33% of 3.03 V. In Li_2MnO_3 phase, a 12.5% doping concentration of V, Nb, Fe, Ru or 4.17% F have the effect of decreasing the redox potential of the 6.25% Li by 0.7~2.5 V. Then, if the doping concentration is increased, so will the amount of Li affected by the dopant. This fact is consistent with our intuition that we can not expect to lower/increase the redox potential with a small amount of doping, which would indicate a completely different material.

c. Ionic conductivity. $LiMnO_2$ and $LiMn_{0.917}M_{0.083}O2$ phase. The Li diffusion coefficient exponentially depends on the kinetic diffusion barrier. In this section, we show the dopant influence on the diffusion barrier. Li ions in $LiMnO_2$ occupy the octahedral sites surrounded by six oxygen atoms. When Li migrates to an adjacent site, it can pass through the space between two oxygen ions, which is known as Oxygen dumbbell hop (ODH), or pass through a tetrahedral site in the middle of the path, which is known as tetrahedral site hop (TSH).[55] The two paths are illustrated in Figure 5. Our calculations show that the ODH path is more energetically favorable, with a diffusion barrier of 0.5 eV which is lower than the TSH path of 0.65 eV. This result can be understood in terms of the strong repulsive coulombic force from the nearest neighbor Li^+ (Li_{NN}) in the transition state of the TSH path. This is also why when this Li_{NN} is removed as shown in Figure 5 the formation of Li vacancy V_{Li}, the TSH path (now marked as TSH-V_{Li} path) has a lower kinetic barrier of 0.35 eV.

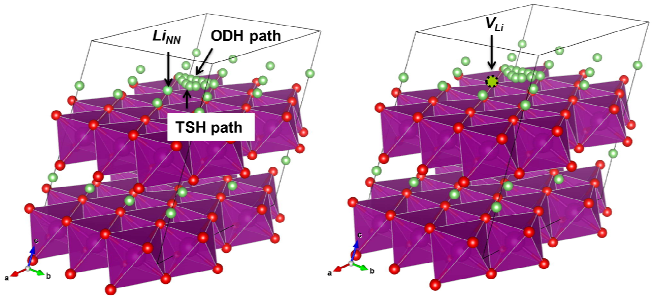

Figure 5. The two paths (ODH and TSH) for Li vacancy diffusion in $LiMnO_2$ without (left) and with (right) a neighbour V_{Li}.

Note that, although $LiMnO_2$ and $LiCoO_2$ share the same layered structure, the Li diffusion behavior shows some differences between them. In $LiCoO_2$, the diffusion barrier of the ODH path is about 0.8 eV, and it is only 0.2 eV for the TSH-V_{Li} path, 0.6 eV lower. However, the difference in $LiMnO_2$ is only 0.15 eV. Two possible reasons account for this difference: one is the smaller resistance when Li diffuses along ODH path in $LiMnO_2$. The octahedral volume occupied by Li ions in $LiMnO_2$ is 13.78 $Å^3$, which is larger than 13.14 $Å^3$ for $LiCoO_2$. This indicates that there is more empty volume available for Li diffusion between two octahedral sites in $LiMnO_2$ and therefore a slight preference for the ODH diffusion path. Also, the nearest neighbor Li-Li distance in $LiMnO_2$ is 3.10 Å, which is larger than 2.91 Å in $LiCoO_2$. On the other hand, Bader charge analysis results in a charge state of $+0.872e^-$ for Li in $LiMnO_2$ and $+0.864e^-$ in $LiCoO_2$, respectively. Combining charge state and atomic distance data, the Coulombic repulsive energy between nearest neighboring Li ions in $LiCoO_2$ is estimated to be roughly 1.114 times larger than in $LiMnO_2$, which will contribute to a more favorable TSH Li diffusion path when a V_{Li} is created in $LiCoO_2$.

Another reason might be the different lattice distortion observed for the two diffusion paths in $LiMnO_2$. Figure S1(a) shows the lattice distortions in the Mn-O bonding during Li migration along the TSH-V_{Li} path in $LiMnO_2$. When the Lithium vacancy is formed, a charge compensation is induced in the surrounding Mn atoms, leading to the result that the nearest neighbor Mn ion transforms from Mn^{3+} into Mn^{4+}, with the subsequent changes in the length of two Mn-O bonds, from ~2.3 Å to 2.0 Å. The lattice distortion is observed in both ODH and TSH-V_{Li} pathways. This interesting behavior is closely related to the Jahn-Teller effect of Mn^{3+}, which is also important for the charge transport as will be discussed in detail latter. In order to quantify the lattice distortion difference between ODH and TSH-V_{Li} paths, we compared the atomic displacements of Mn and O atoms when Li diffuses from the initial state to the saddle point (in the middle of the diffusion path) of each path. Larger atomic displacements indicate larger lattice distortions due to Li diffusion. As shown in Fig. S2, larger Mn and O displacements were obtained for the ODH path. For the TSH-V_{Li} path, only O displacements were observed. This finding indicates that the $LiMnO_2$ lattice undergoes a larger distortion when Li diffuses along ODH path, which lowers the total energy of saddle point and therefore the diffusion barrier.

Table 1. The Li vacancy diffusion barriers in doped $LiMnO_2$. The diffusion barrier in pure $LiMnO_2$ is 0.50 eV.

Dopants	Diffusion Barrier (eV)	Dopants	Diffusion Barrier (eV)
Mg	0.42	Co	0.43
Ti	0.42	Ni	0.27
V	0.42	Cu	0.48
Nb	0.50	Al	0.79
Fe	0.45	N	0.78
Ru	0.43	F	0.68

Since our main goal is to understand the influence of the dopants on the diffusion barriers, we therefore focus on how the external dopants affect the diffusion along the ODH pathway. The doping site along the ODH path is illustrated in Figure S1(b) and the obtained kinetic barriers are listed in Table 1, which shows that most of the cationic dopants lower the diffusion barrier, but only by less than 0.1 eV. Two remarkable exceptions are Ni, which decreases the barrier by 0.23 eV, and Al, which largely increases the barrier by 0.3 eV. Both N and F also increase the barrier by 0.28 eV and 0.18 eV respectively. The mechanism of how these dopants influence the diffusion barrier may be understood from the Jahn-Teller effect of Mn^{3+}. Previous discussion has shown that strong lattice distortion happens along Li diffusion path and the distortion at the transition state will influence the diffusion barrier. Figure 6 shows the distortions of Mn_{NN}-O (Mn_{NN} is illustrated in Figure S1(b)) bonds in the transition state for pure $LiMnO_2$ and three doped phases. In pure $LiMnO_2$ without any Lithium vacancy, two Mn-O bonds are elongated to be ~2.3 Å and the other four are kept at ~2.0 Å because of Jahn-Teller effect. As shown in Figure 6, when Li is migrating in pure $LiMnO_2$, two long Mn-O bonds of one Mn_{NN} are shorten back to 2.0 Å. But with Ni doping, the long Mn-O bonds of both two Mn_{NN} are shorten back, but no long Mn-O bonds are shorten in Al and F doped phases. These results indicate that Ni facilitates the suppression of the Jahn-Teller distortion and the transition state experiences large structure relaxation during Li migration, which leads the structure to a lower barrier. Meanwhile, Al and F keep the Mn-O bond distortion of pure $LiMnO_2$, and the transition state undergoes no additional structure relaxation, therefore raising the diffusion barrier.

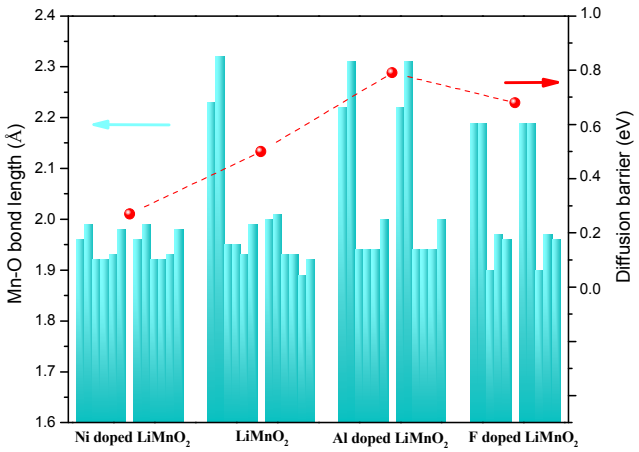

Figure 6. Mn-O bond length distributions of two Mn_{NN} in the Li diffusion ODH path transition states of pure $LiMnO_2$, Ni, Al and F doped $LiMnO_2$ phases and the corresponding diffusion barriers.

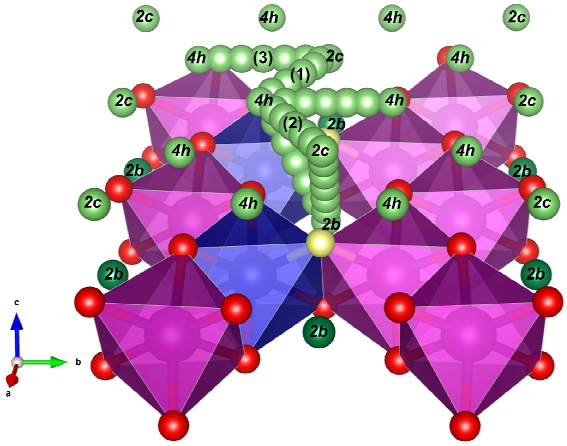

Figure 7. Li vacancy diffusion paths in doped Li_2MnO_3. Purple, dark green, light green and red atoms represent Manganese, Lithium in Li-layer, Lithium in Li-Mn mixed-layer and Oxygen respectively. Blue and Yellow mark the cation and anion doping sites. 2c, 2b and 4h are the different Li vacancy sites. (1), (2) and (3) are used to differentiate the three different 4h↔2c paths.

Li_2MnO_3 and $Li_2Mn_{0.875}M_{0.125}O_3$ phase. Ionic diffusion in Li_2MnO_3 is more complex, due to the appearance of both interlayer (2b-2c, 2b-4h) and intralayer (2c-4h, 4h-4h) diffusion pathways. The diffusion between 4h and 2c sites is also divided into 3 different pathways, depending on their distances to the dopants, as shown in Figure 7. A summary of Li vacancy diffusion barriers in pure and doped Li_2MnO_3 is listed in Table 2. Because of the asymmetric initial and final Li vacancy sites, the diffusion barriers are direction dependent. In the pure Li_2MnO_3 phase, for V_{Li} diffusion from 2b site to 2c or 4h, i.e., Li diffusion from a Li-layer to a Li-Mn mixed-layer, the barriers are all around 0.5 eV. But when the V_{Li} diffuses back, the barriers are 0.11~0.16 eV higher. Intralayer diffusion generally shows barriers around 0.6 eV, except for the 2c-4h diffusion along *b* direction, which are about 0.8 eV. Because of the complex pathways in Li_2MnO_3, the dopants show different effects on the diffusion paths. Overall, Mg, Ti, V, Nb, Fe, Ru and Co can facilitate the interlayer diffusion. Among these dopants, Nb shows the most remarkable influence, decreasing the barrier of V_{Li} from 2c and 4h to the 2b site by 0.26 eV and 0.29 eV, respectively. This result indicates that Nb doping will strongly activate the Li atom diffusion in Li-Mn mixed-layers. On the other hand, Mg, Ti, V, Nb, Fe, Ru, Ni, Al and N can facilitate the intralayer diffusion, whereas Mg, Ru and Al lower the kinetic barriers of the three paths between 2c and 4h sites.

Table 2. The Li vacancy diffusion barriers in doped Li_2MnO_3 relative to pure Li_2MnO_3. A→B means Li vacancy will diffuse from the A site to B site.

	Interlayer diffusion (eV)				Intralayer diffusion (eV)						
Dopant	2b→2c	2c→2b	2b→4h	4h→2b	2c→4h (1)	4h→2c (1)	2c→4h (2)	4h→2c (2)	2c→4h (3)	4h→2c (3)	4h↔4h
Li_2MnO_3	0.52	0.63	0.51	0.67	0.57	0.61	0.56	0.60	0.76	0.80	0.58
Mg	-0.05	-0.06	+0.02	-0.10	-0.07	-0.05	-0.11	-0.09	-0.05	-0.08	
Ti	-0.04	-0.08	-0.01	-0.13	-0.05	-0.06	-0.09	-0.10	+0.02	+0.01	
V	+0.02	-0.04	+0.02	-0.14	-0.09	-0.08	0.00	+0.01	-0.06	-0.10	
Nb	-0.04	-0.26	+0.02	-0.29	-0.06	-0.06	-0.09	-0.09	+0.01	-0.03	
Fe	0.00	-0.03	-0.03	-0.02	-0.10	-0.05	+0.04	+0.09	-0.08	-0.10	
Ru	-0.06	-0.06	0.00	-0.12	-0.08	-0.09	-0. 08	-0.08	-0.06	-0.08	
Co	-0.06	+0.06	-0.08	-0.19	+0.12	+0.04	-0.01	-0.01	+0.01	-0.03	
Ni	0.00	+0.06	-0.01	+0.09	-0.04	+0.01	-0.05	0.00	-0.10	-0.09	
Cu	-0.03	+0.01	-0.04	+0.10	-0.10	+0.01	+0.03	+0.14	-0.11	-0.11	
Al	+0.03	-0.01	+0.03	-0.08	-0.02	-0.04	-0.02	-0.04	-0.04	-0.05	
N	-0.14	-0.06	+0.26	+0.13	+0.02	+0.13	-0.25	-0.14			-0.06
F	-0.09	+0.04	+0.08	+0.08	+0.02	+0.01	-0.08	-0.09			-0.05

d. Electronic conductivity. $LiMnO_2$ phase. If we remove an electron from the $LiMnO_2$ phase, the extra hole will be trapped by the lattice distortion and form a small polaron due to the Jahn-Teller effect of Mn^{3+}. In $LiMnO_2$, the Mn atoms are bound to O ions in an octahedral cage formed by 6 O atoms, with their five *d* orbitals split into 3 t_{2g} orbitals with lower energy and 2 e_g orbitals with higher energy. According to the Hund rules, 3 electrons of Mn^{3+} occupy the t_{2g} orbitals with the same spin, and the other electron will occupy a twofold degenerate e_g orbital. Therefore, the lattice distortions eliminate this degeneracy, leading the system to a more stable energy state. This effect has been shown in many Mn oxides, such as $LaMnO_3$, $LiMn_2O_4$ and $LiMnO_2$, and plays an important role in determining their properties.[57,58,59] In the current $LiMnO_2$ layered structure, each Mn atom is bound to 6 O, with four Mn-O bonds showing a similar length of 2.0 Å, and the other two Mn-O bonds stretched to 2.3 Å, which is consistent with a Jahn-Teller lattice distortion.

When one extra hole is introduced into our $Li_{24}Mn_{24}O_{48}$ model, the two stretched 2.3 Å Mn-O bonds shorten to 2.0 Å after the structural relaxation. Figure 8 shows the charge density difference between pure $LiMnO_2$ and $LiMnO_2$ with an extra hole. The hole is localized on one of the Mn^{3+} atoms, which therefore transforms into Mn^{4+}. Four d electrons of Mn^{3+} now occupy 3 t_{2g} orbitals and 1 e_g orbital in a high-spin state. When Mn^{4+} forms, one of the energetically higher e_g electrons is extracted, as shown in the density of states (DOS) plotted in Figure 8, where one of the spin-up states is pushed above the Fermi level. The quasiparticle formed by the hole and the lattice distortion induced in its surrounding is called a hole polaron. The transportation of holes in $LiMnO_2$ is therefore coupled with the migration of polarons, indicating that when an electron is migrating between two different sites, the motion will drag a series of lattice distortions which ultimately increase the motion resistance. As this migration process exponentially depends on the activation energy, i.e., the migration barrier, we obtained the energy barrier for the migration of a hole polaron between two neighboring sites.

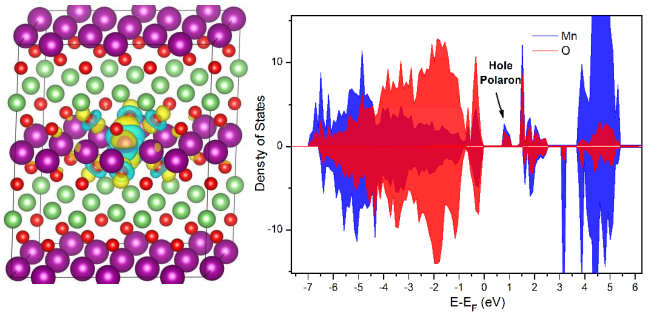

Figure 8. The density of states (right) and charge density (left) of the hole polaron in $LiMnO_2$.

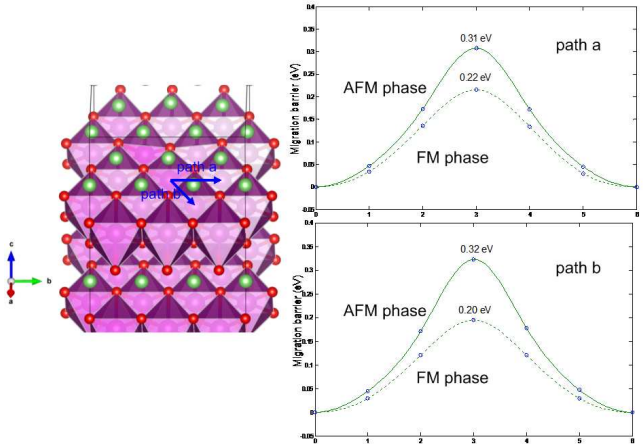

Figure 9. The diffusion paths (a and b) and corresponding barriers for hole polaron diffusing between nearest neighbor positions.

Figure 9 shows the two considered pathways and the corresponding migration barriers. According to our results, $LiMnO_2$ is more stable in the antiferromagnetic (AFM) phase, and the kinetic energy barriers along the two paths are 0.31 eV and 0.32 eV. If we consider the ferromagnetic (FM) phase, the kinetic barriers decrease by about 0.1 eV. This fact can be understood in terms of the double-exchange mechanism, where an electron migrates between two Mn atoms through an O network, being the process more favorable if the spins of the two neighboring Mn atoms are aligned in the same direction.

During the initial discharge cycle, the migration of the polaron may be affected by neighboring Li vacancies. Previous reports on the study of polarons in $LiFePO_4$ and $LiMnPO_4$ indicate that the barrier is increased by about 0.1 eV if there are some neighboring Li vacancies.[60] We therefore considered two different situations in order to analyze the influence of vacancies on the polaron migration (see Figure 10): in one case the Li vacancy is sitting in the middle of the path and in the other case, the vacancy is close to the end of the path. However, our results show that, for $LiMnO_2$, the influence of Li vacancies on the hole polaron migration barrier is almost negligible, and the barrier is increased by only 20 meV (path a) or remains constant (path b) .

Unlike hole polarons, electron polarons are not observed in $LiMnO_2$, indicating that the electrons will be transported through the Conduction Band Minimum (CBM) following rigid-band theory. The parabolic curvature of CBM between each high symmetric K points (as shown in Figure S3) also indicates the light electronic effective mass. Consequently, as long as free electrons are generated in $LiMnO_2$, the electronic mobility should be relatively high. Based on the above understanding, the strategy for improving electronic

conductivity of $LiMnO_2$ should be the inhibition of hole polaron formation or the introduction of shallow n-type doping.

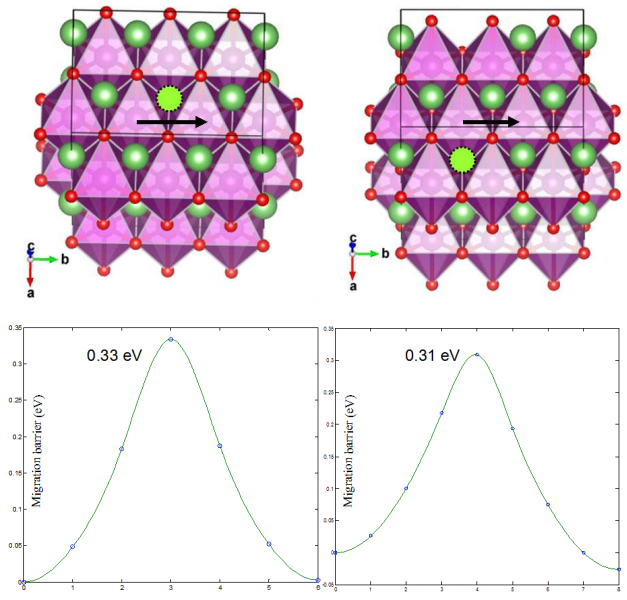

Figure 10. The hole polaron diffusion barriers with different Li vacancy environments.

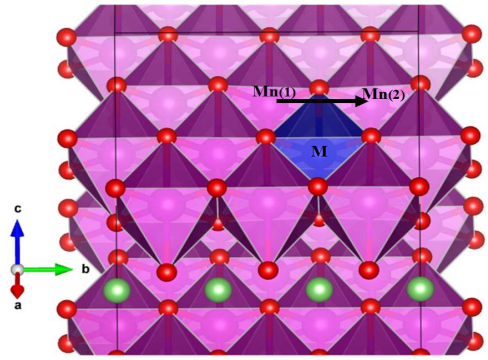

Figure 11. Hole polaron migration paths, from Mn(1) to Mn(2), in M doped $LiMnO_2$.

Doped $LiMnO_2$ phase. In this section, we will discuss how the dopants influence the behaviors of hole polaron in $LiMnO_2$. Figure 11 shows the model used in our calculations of the hole polaron in doped $LiMnO_2$, where Mn(1) and Mn(2) are the two nearest neighbor polaron sites of the dopant M, set as the initial and final positions of the migration path. Mg doping shows no influence on the polaron properties, with a migration barrier of 0.30 eV. After relaxation of the other doped phases with an extra hole, no polaron formation is observed, which indicates that all the considered dopants inhibit the polaron formation. However, if we provide an initial perturbation to the Mn-O bonds before relaxation, the hole polaron is formed for the Fe, Co, Al, Ni and Cu doped phases. The charge distribution difference is illustrated in Figure S4, taking Al doping as an example. When the polaron is not formed, the hole is distributed evenly in the whole structure, i.e., in the VBM, but when the polaron forms, the hole is localized on a certain Mn site, which also leads the structure to a more stable state. Table 3 lists the energy differences, which range from 11.2 meV/unit cell to 30.7 meV/unit cell. Among the dopants considered in our study, Fe shows almost no influence on the migration barrier. Co and Al reduce the kinetic barrier by 0.05 eV and 0.04 eV, respectively. Assuming a simple Arrhenius relation for the electronic conductivity, this reduction of the energy barrier could improve the hole conductivity up to 7 times. Ni and Cu show specific features, because we found the formation of two polarons at two nearest neighbor Mn sites of the dopant even though there is only one extra hole in the system. This leads the $LiMnO_2$ doped phase into a much more stable energy configuration, 30.7 (Ni) and 25.6 (Cu) meV/unit cell lower in total energy than the phase without polaron formation. The polaron migration barriers are also increased by 0.04 eV and 0.05 eV for Ni and Cu, respectively. On the other hand, no polaron can be formed in the Ti, V, Nb and Ru doped phases, even if an initial perturbation is provided. From this point of view, these 4 dopants can be viewed as good candidates to

Table 3. The hole polaron formation state (*Y* represents form and *N* represents not form), polaron migration barrier E_b, Energy difference ΔE ($\Delta E = E_{\text{phase without polaron}} - E_{\text{phase with polaron}}$) and doping type in pure $LiMnO_2$ and doped $LiMnO_2$.

Dopant	State (*Y*/*N*)	E_b(eV)	ΔE (meV/unit)	Doping type[a]
$LiMnO_2$	*Y*	0.31	-	-
Ti	*N*	-	-	*D-n*
V	*N*	-	-	*D-p*
Nb	*N*	-	-	*D-n*
Ru	*N*	-	-	*D-n*
Mg	*Y*	0.30	-	*S-p*
Fe	*Y*	0.30	14.3	*D-p*
Co	*Y*	0.26	11.2	*D-p*
Al	*Y*	0.27	12.3	*D-p*
Ni	*Y*	0.35	30.7	*D-p*
Cu	*Y*	0.36	25.6	*D-p*

[a] *S-p*: Shallow p-tpye; *S-n*: Shallow n-type; *D-p*: Deep p-type; *D-n*: Deep n-type

inhibit the hole polaron formation. As also shown in Table 3, no dopant is found to be shallow n-type doping and Mg is shallow p-type doping.

Based on the charge transportation mechanism we proposed and the different doping effects we discussed, the influences of dopants can be summarized as follows: Ti, V, Nb, Ru can inhibit the hole polaron formation and therefore increase the hole conductivity. Although Co and Al do not inhibit polaron formation, they slightly decrease the polaron migration barrier, which may increase the hole conductivity up to 7 times. Mg, Fe, Ni, Cu do not inhibit polaron formation and, among them, Ni and Cu even increase the polaron migration barrier, and Mg introduces shallow p-type doping. Therefore, these four dopants may even lower the electronic conductivity.

Li_2MnO_3 phase. Similarly to the hole polaron formation in $LiMnO_2$, an electron polaron can be formed in Li_2MnO_3 (with the subsequent reduction of Mn^{4+} to Mn^{3+}). But the process is slightly different: when one electron is added to the $Li_{32}Mn_{16}O_{48}$ model, the formation of an electron polaron is not observed, even though an initial perturbation was introduced in the Mn-O bonds. However, if two electrons are added to the Li_2MnO_3 phase, the system tends to form two electron polarons (after the corresponding initial perturbation in the Mn-O bonds), with an energy of 25.6 meV/unit cell lower than that of the phase without polarons. In the laboratory, the initial perturbation required to activate the polaron formation might be achieved through thermodynamic vibrations, with an estimated activation energy of only 0.05 eV. The charge density of the two polarons is shown in Figure 12, where the two polarons (p1 and p2) are found to be more stable if staying at different layers. The two-center bipolaron (TCBP) phenomenon observed in the current materials has been widely studied in some semiconductors, ionic crystals and high-temperature superconductors.[61,62,63,64] Understanding of TCBP is often done through the hydrogen molecule or Deigen's F_2-center model, in which the polaron wells play the role of positively charged nuclei.[64] The exchange interactions between polaron electrons in the singlet state will attract the neighboring polarons and stabilize the bipolaron system, whereas Coulomb repulsion will keep the polarons at a proper distance. This may be the reason why, in our case, two polarons are found to be more stable at different layers (as compared to staying at the same layer), because the repulsion interaction would be overridden by the exchange interaction and the balance of these two interactions will finally stabilize the polarons at different layers. On the other hand, by observing the charge density (the integral of the squared wave-functions) in Figure 12, it can be noted that O is stretched into the Li-layer due to elongation of Mn-O bonding after the formation of an electron polaron. This will facilitate the overlapping between the wave-functions of the two polarons or, in other words, the exchange interaction in Li_2MnO_3 is more non-negligible, which would be the reason why bipolaron formation is unexpectedly more favorable. To obtain the kinetic migration barrier, we fix p2 and allow p1 to migrate to its nearest neighboring site. The obtained barrier (see Figure 12) is about 0.20 eV, 0.11 eV lower than that of the hole polaron migration barrier obtained for the AFM $LiMnO_2$ phase, but similar to the one obtained for the FM $LiMnO_2$ phase. The Li_2MnO_3 phase is more stable in the FM state, and these two polaron migrations can therefore be viewed as mirrored processes (Mn^{4+} reduces to Mn^{3+} and Mn^{3+} oxidizes to Mn^{4+}) in the same magnetic configuration.

On the other hand, the formation of hole polarons is not observed, indicating that the hole carrier will be transported through the VBM. Figure S5 gives the band structure of Li_2MnO_3, which also shows the parabolic curvature between high-symmetry K points in the valence band, indicating the light effective mass of the hole. Contrary to $LiMnO_2$, the strategy for improving electronic conductivity of Li_2MnO_3 should be the inhibition of electron polaron formation and also the introduction of shallow p-type doping.

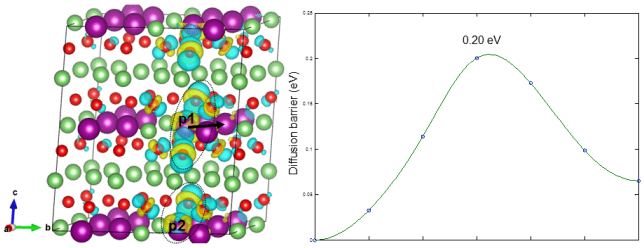

Figure 12. Charge density of electron polaron in Li_2MnO_3 and its diffusion barrier to neighboring position.

Doped Li_2MnO_3 phase. Table 4 summarizes our obtained results on polaron formation for the doped Li_2MnO_3 phase. Our goal is to analyze whether the formation of both p1 and p2 polarons can be inhibited by doping and how the migration of one of the polarons is affected by the presence of the other one (see the model in Figure S6a). Our results show that Mg, Ru and Ni inhibit the formation of both polarons. On the contrary, Nb, Fe, Co, Cu and Al partially inhibit the electron polaron formation. Taking Al as an example, the electron density distribution (see Figure S6b) shows that a polaron is formed in an undoped Li-Mn mixed layer and another one is evenly distributed in the CBM. This finding shows that the formation of p1 is inhibited by Nb, Fe, Cu, Co and Al, but not p2, also indicating that the doping effect on polaron formation is restricted to the layer where the impurity is located. The migration barrier of p2 is hardly altered by the doping, due to the large distance between the polaron and the impurity (see Figure S6a and Table 4). Finally, Ti and V doping will allow the polaron formation, but with an increase in the migration barrier of 0.02 eV and 0.10 eV respectively. Table 4 also

shows that all the dopants considered in this work increase the energy difference with respect to the Li_2MnO_3 phase without polarons (by amount between 1.8 and 53.7 meV/unit cell), thus contributing to stabilize the polaronic structures.

Among the dopants, Mg, Ru can Ni can inhibit the electron polaron formation in Li_2MnO_3, with Mg also showing shallow p-type doping, which will facilitate the hole transport. This is also consistent with the experimental observation that, by 15% Ru doping (substituting Mn), the conductivity of Li_2MnO_3 can be increased by 10^4 times.[22] Co, Al, Cu, Nb and Fe partially inhibit the polaron formation, i.e., their effects are localized within the doping layer. Al and Fe also show shallow p-type doping, indicating that although they can not totally inhibit electron polaron formation, they can introduce more conductive holes. Finally, Ti and V were found to stabilize the polaron formation structure, and also to increase the migration barrier.

Table 4. The electron polarons formation state (*Y* represents form, *N* represents not form and *Y*/*N* represents partly form), polaron migration barrier E_b, Energy difference ΔE ($\Delta E = E_{\text{phase without polaron}} - E_{\text{phase with polaron}}$) and doping type in pure Li_2MnO_3 and doped Li_2MnO_3.

Dopant	State (*Y*/*N*)	E_b(eV)	ΔE (meV/unit)	Doping type[a]
Li_2MnO_3	*Y*	0.20	25.6	-
Mg	*N*	-	-	*S-p*
Ru	*N*	-	-	*D-n*
Ni	*N*	-	-	*D-p*
Co	*Y/N*	0.20	27.4	*D-p*
Al	*Y/N*	0.20	35.6	*S-p*
Cu	*Y/N*	0.20	58.6	*D-p*
Nb	*Y/N*	0.20	61.4	*D-n*
Fe	*Y/N*	0.20	79.3	*S-p*
Ti	*Y*	0.22	64.0	*D-p*
V	*Y*	0.30	68.5	*D-p*

[a] *S-p*: Shallow p-tpye; *S-n*: Shallow n-type; *D-p*: Deep p-type; *D-n*: Deep n-type

Another important point is, as not all the charge carriers can form polarons, what is the main carrier in both $LiMnO_2$ and Li_2MnO_3. If we consider only a realistic charging process, the Li^+ ion will be firstly extracted and enter the surrounding electrolyte, leaving an extra electron in the cathode, which will go across the cathode to finally enter in the external circuit. At the same time, because of the large band gaps of both oxides (1.58 eV for Li_2MnO_3 and 1.64 eV for $LiMnO_2$ as shown in Figures S2 and S4), thermal excited hole/electron pairs are difficult to create. In this sense, although polarons were found to be formed in both oxides, the main charge carriers should be electrons during the charging process. This may be the reason why, although both oxides have relatively low electronic conductivity, but conductivity of $LiMnO_2$ phase ($10^{-4} \sim 10^{-5}$ S/cm) is still much larger than that of the Li_2MnO_3 phase (10^{-9} S/cm).

CONCLUSIONS

In this study, we have examined in detail the influence of 10 cationic (Mg, Ti, V, Nb, Fe, Ru, Co, Ni, Cu, Al) and 2 anionic (N, F) dopants on the redox potential, ionic and electronic conductivities of both $LiMnO_2$ and Li_2MnO_3 cathode materials. Our results show that all the cationic and F doped phases are thermodynamically stable with negative heats of formation. N doped phase is not stable from a thermodynamic point of view, due to the strong binding between N atoms. 8.33% Mg, Ti, V, Ru or 4.17% F dopants decrease the redox potential of $LiMnO_2$ for the 8.33% Li by 0.4~1.0 V and Nb for the 16.67% Li by 2.70~3.03V. On the other hand, 12.5% V, Nb, Fe, Ru or 4.17% F also strongly lowers the redox potential of 6.25% Li in the Li_2MnO_3 phase by 0.7~2.5 V. These results can be a reference in considering doping concentration in realistic application. The so-called ODH pathway is energetically more favorable for Li vacancy diffusion, with a migration barrier of 0.5eV, and most of the considered dopants decrease that barrier, except Nb, Al, N and F. Li vacancy diffusion in Li_2MnO_3 is a bit more complex, due to the availability of more diffusion paths. Our results show that Mg, Ti, V, Nb, Fe, Ru and Co facilitate the interlayer diffusion, whereas Mg, Ti, V, Nb, Fe, Ru, Ni, Al and N can promote the intralayer diffusion. With respect to the electronic conductivity, hole polarons and electron polarons are formed in the $LiMnO_2$ and Li_2MnO_3 phases, respectively, due to the Jahn-Teller effect of the Mn^{3+}. The influence of dopants on charge conductivity can be derived through their influence on polaron migration barrier. If the dopants inhibit the polaron formation, there is no barrier for charge migration. The hole polaron migration barrier in $LiMnO_2$ is 0.31 eV; the hole conductivity can therefore be increased by about 10^6 times if the polaron formation is inhibited. For Li_2MnO_3, the electron polaron migration barrier is 0.2 eV. Thus, the inhibition of polaron formation will increase the electron conductivity by $2x10^4$ times. In $LiMnO_2$, Ti, V, Nb, Ru can improve the conductivity through inhibiting hole polaron formation. Co and Al slightly lower the polaron migration barrier and Mg, Fe, Ni and Cu might further lower the electronic conductivity as they increase the migration barrier or introduce shallow p-type doping. For the Li_2MnO_3 phase, Mg, Ru and Ni can inhibit the formation of electron polarons and increase the conductivity, and Mg also shows shallow p-type doping,

increasing hole concentration. Co, Al, Cu, Nb and Fe only partly inhibit polaron formation, and their ability to improve the conductivity is then limited. But, among them, Al and Fe are also shallow p-type dopants, indicating the hole conduction can be activated. Ti and V are not the best candidates to improve the electronic conductivity, as they stabilize the polaron formation and increase the polaron migration barrier.

ASSOCIATED CONTENT

Supporting Information. Formation energy of doped spinel and layered lithiated manganese oxides, redox potential of doped $LiMnO_2$ and Li_2MnO_3 with different Li concentration, lattice distortions during Li diffusion in $LiMnO_2$, doping position relative to ODH diffusion path in $LiMnO_2$, Mn and O displacements along different diffusion paths, band structures of $LiMnO_2$ and Li_2MnO_3, and partial charge density of Al doped Li_2MnO_3. This material is available free of charge via the Internet at http://pubs.acs.org.

AUTHOR INFORMATION

Corresponding Author

* E-mail: kjcho@utdallas.edu (KJ. Cho), sgdoo@samsung.com (S. Doo)

ACKNOWLEDGMENT

This work was supported by Samsung GRO project. The authors also acknowledge the Texas Advanced Computing Center (TACC) for providing computational resources.

REFERENCES

1 K. Mizushima, P. C. Jones, P. J. Wiseman, J. B. Goodenough, *Mater. Res. Bul.*, 1980, **15**, 783.
2 J. N. Reimers, J. R. Dahn, *Electrochem. Soc.*, 1992. **139,** 2091.
3 P. Kalyani, N. Kalaiselvi, *Science and Technology of Advanced Materials*, 2005, **6**, 689.
4 T. Ohzuku, A. Ueda, M. J. Nagayama, *Electrochem. Soc.*, 1993, **140**, 1862.
5 U. Sacken, M. W. Juzkow, H. Al-Janaby, *J. Electrochem. Soc.*, 1991, **138**, 2207.
6 M. V. Reddy, B. D. Tung, L. Yang, N. D. Q. Minh, K. P. Loh, B. V. R. Chowdari, *Journal of Power Sources*, 2013, **225**, 374.
7 P. Y. Liao, J. G. Duh, H. S. Sheu, *Electrochemical and Solid-State Letters*, 2007, **10**, A88.
8 T. Ohzuku, Y. Makimura, *Chemistry Letters.*, 2001, **8**, 744.
9 K. Zaghib, A. Mauger, C. M. Julien, *J Solid State Electrochem*, 2012, **16**, 835.
10 A. K. Padhi, K. S. Nanjundaswamy, J. B. Goodenough, *J. Electrochem. Soc.*, 1997, **144**, 1188.
11 A. Yamada, S. C. Chung, K. Hinokuma, *Journal of The Electrochemical Society*, 2001, **148**, A224.
12 M. M. Thackeray, C. S. Johnson, J. T. Vaughey, N. Li, S. A. Hackney, *J. Materials Chemistry*, 2005, **15**, 2257.
13 A. D. Robertson, P. G. Bruce, *Chem. Mater.*, 2003, **15**, 1984.
14 A. D. Robertson, P. G. Bruce, *Chem. Commun.*, 2002, 2790.
15 N. Tran, L. Croguennec, M. Menetrier, F. Weill, Ph. Biensan, C. Jordy, C. Delmas, *Chem. Mater.*, 2008, **20**, 4815.
16 A. R. Armstrong, M. Holzapfel, P. Novak, C. S. Johnson, S.-H. Kang, M. M. Thackeray, P. G. Bruce, *J. Am. Chem. Soc.*, 2006**, 128**, 8694.
17 N. Yabuuchi, K. Yoshii, S.-T. Myung, I. Nakai, S. Komaba, *J. Am. Chem. Soc.*, 2011, **133**, 4404.
18 H. Koga, L. Croguennec, M. Menetrier, K. Douhil, S. Belin, L. Bourgeois, E. Suard, F. Weill, C. J. Delmas, *Electrochem. Soc.*, 2013, **160**, A786.
19 P. Suresh, A. K. Shukla, N. Munichandraiah, *Journal of Power Sources*, 2006, **161**, 1307.
20 X. M. Wu, R. X. Li, S. Chen, Z. Q. He, M. F. Xu, *Bull. Mater. Sci.*, 2008, **31**, 109.
21 S. Kim, J.-K. Noh, S. Yu, W. Chang, K. Y. Chung, B.-W. Cho, *J Electroceram*, 2013, **30**, 159.
22 D. Moria, H. Sakaebeb, M. Shikanob, H. Kojitania, K. Tatsumib, Y. Inaguma, *Journal of Power Sources*, 2011, **196**, 6934.
23 M. Sathiya, K. Ramesha, G. Rousse, D. Foix, D. Gonbeau, A. S. Prakash, M. L. Doublet, K. Hemalatha, J.-M. Tarascon, *Chem. Mater.* 2013, **25**, 1121.
24 S. Lee, S. Choi, J. Kim, H. Sim, C. Won, S. Lee, S. A. Kim, N. Hur, J.-G. Park, *J. Phys. Condens. Matter*, 2012, **24**, 456004.
25 P. K. Sharma, G. J. Moore, F. Zhang, P. Zavalij, M. S. Whittingham, *Electrochemical and Solid-State Letters*, 1999, **2**, 494.
26 A. K. Padhi, K. Nanjundaswamy, J. B. Goodenough, *J. Electrochem. Soc.*, 1997, **144**, 1188.
27 S. Levasseur, M. Menetrier, C. Delmas, *Chem. Mater.*, 2002, **14**, 3584.
28 J. Molenda, P. Wilk, J. Marzec, *Solid State Ionics*, 2002, **146**, 73.
29 J. V. Elp, J. L. Wieland, H. Eskes, P. Kuiper, G. A. Sawatzky, F. M. F. de Groot, T. S. Turner, *Phys. Rev. B*, 1991, **44**, 6090.
30 G. Kresse, J. Hafner, *Phys. Rev. B*, 1993, **47**, 558.
31 G. Kresse, J. Furthmuller, *Comput. Mater. Sci*. 1996, **6**, 15.
32 G. Kresse, D. Joubert, *Phys. Rev. B*, 1999, **59**, 1758.
33 J. P. Perdew, K. Burke, M. Ernzerhof, *Phys. Rev. Lett.*, 1997, **78**, 1396.
34 P. E. Blöchl, O. Jepsen, O. K. Anderson, *Phys. Rev. B*, 1994, **49**, 16223.
35 S. L. Dudarev, G. A. Botton, S. Y. Savrasov, C. J. Humphreys, A. P. Sutton, *Phys. Rev. B*, 1998, **57**, 1505.
36 D. O. Scanlon, B. J. Morgan, G. W. Watson, *The Journal of Chemical Physics*, 2009, **131**, 124703.
37 F. Zhou, M. Cococcioni, C. A. Marianetti, D. Morgan, G. Ceder, Phys. Rev. B, 2004, **70**, 235121.
38 R. Xiao, H. Li, L. Chen, *Chem. Mater.*, 2012, **24**, 4242.
39 P.-A. Lin, H.-T. Jeng, C.-S. Hsue, *Phys. Rev. B*, 2008, **77**, 085118.
40 B. J. Morgan, G. W. Watson, *Phys. Rev. B*, 2010, **82**, 144119.
41 L. Wang, T. Maxisch, G. Ceder, *Phys. Rev. B*, 2006, **73**, 195107.
42 B. J. Morgan and G. W. Watson, *Surf. Sci.*, 2007, **601**, 5034.
43 G. Hautier, S. P. Ong, A. Jain, C. J. Moore, G. Ceder, *Phys. Rev. B*, 2012, **85**, 155208.
44 W. Zhang, W. Wu, X. Wang, X. Cheng, D. Yan, C. Shen, L. Peng, Y. Wang, L. Bai, *Surf. Interface Anal.* 2013, **45**, 1206.
45 A. O'Hara, T. N. Nunley, A. B. Posadas, S. Zollner, A. A. Demkov, *J. Appl. Phys.*, 2014, **116**, 213705.
46 T. Tamura, T. Ohwaki, A. Ito, Y. Ohsawa, R. Kobayashi, S. Ogata, *Modelling Simul. Mater. Sci. Eng.*, 2012, **20**, 045006.
47 W.-J. Son, P. Manuel, D. Adroja, M.-H. Whangbo, *Inorg. Chem.*, 2011, **50**, 9400.
48 K. Momma, F. J. Izumi, *Appl. Crystallogr.*, 2011, **44**, 1272.

49 G. Henkelman, B. P. Uberuaga, H. J. Jónsson, *Chem. Phys*., 2000, **113**, 9901.
50 M. Tabuchi, Y. Nabeshima, T. Takeuchi, H. Kageyama, J. Imaizumi, H. Shibuya, J. Akimoto, *Journal of Power Sources*, 2013, **221**, 427.
51 T.-J. Kim, D. Son, J. Cho, B. Park, *Journal of Power Sources*, 2006, **154**, 268.
52 I. R. Mangani, W. Y. Cho, J. Kim, *Ionics*, 2007, **13**, 479.
53 J. Heyd, G. E. Scuseria, M. Ernzerhof, *J. Chem. Phys*. 2003, **118**, 8207.
54 Z. F. Huang, H. Z. Zhang, C. Z. Wang, D. P. Wang, X. Meng, X. Ming, G. Chen, *Solid State Sciences*, 2009, **11**, 271.
55 Y. Okamoto, *Journal of The Electrochemical Society*, 2012, **159**, A152.
56 A. Van der Venz, G. Ceder, *Electrochemical and Solid-State Letters*, 2000, **3**, 301.
57 W. E. Pickett, D. J. Singh, *Phys. Rev. B*, 1996, **53**, 1146.
58 J. B. Goodenough, A. Manthiram, B. Wnetrzewski, *Journal of Power Sources*, 1993, **43**, 269.
59 R. Prasad, R. Benedek, A. J. Kropf, C. S. Johnson, A. D. Robertson, P. G. Bruce, M. M. Thackeray, *Phys. Rev. B*, 2003, **68**, 012101.
60 S. P. Ong, V. L. Chevrier, G. Ceder, *Phys. Rev. B*, 2011, **83**, 075112.
61 P. A. Wolff, R. N. Bhatt, A. C. Durst, *J. Appl. Phys*., 1996, **79**, 5196.
62 N. I. Kashirina, V. D. Lakhno, V. V. Sychyov, *Phys. Rev. B*, 2005, **71**, 134301.
63 D. M. Larsen, *Phys. Rev. B*, 1981, **23**, 628.
64 N. I. Kashirina, V. D. Lakhno, *Physics-Uspekhi*, 2010, **53**, 431.

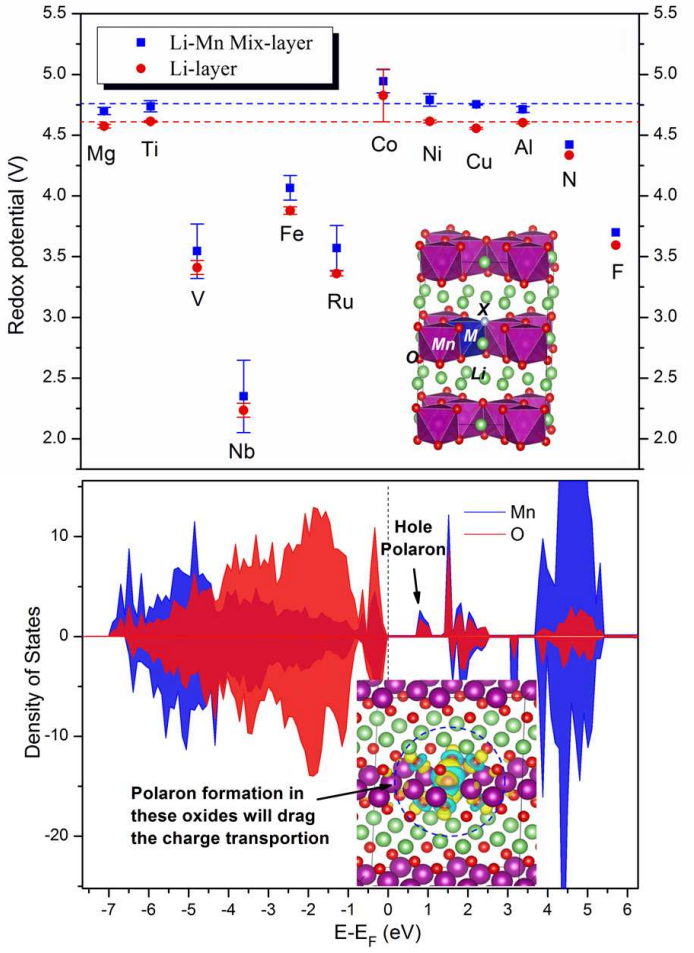

Table of Contents artwork